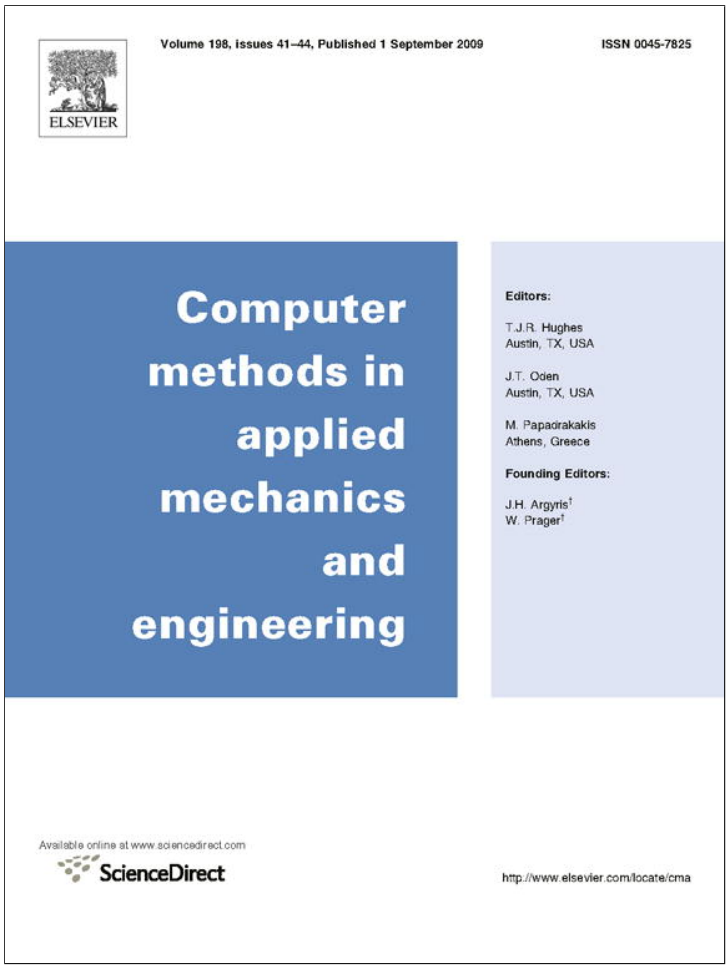

Comput. Methods Appl. Mech. Engrg. 198 (2009) 3400–3410

Contents lists available at ScienceDirect

Comput. Methods Appl. Mech. Engrg.

journal homepage: www.elsevier.com/locate/cma

A consistent reflected image particle approach to the treatment of boundary conditions in smoothed particle hydrodynamics

F. Bierbrauer, P.C. Bollada, T.N. Phillips *

School of Mathematics, Cardiff University, Cardiff CF24 4AG, UK

ARTICLE INFO

Article history:
Received 15 February 2008
Received in revised form 16 June 2009
Accepted 24 June 2009
Available online 30 June 2009

Keywords:
Smoothed particle hydrodynamics
Boundary conditions
Image particle
Newtonian fluid
Poiseuille flow
Couette flow

ABSTRACT

The particle deficiency problem in the presence of a rigid wall for smoothed particle hydrodynamics (SPH) is considered. The problem arises from insufficient information being available to perform accurate interpolation of data at particles located nearer to the boundary than the support of the interpolation kernel. The standard method for overcoming this problem is based on the introduction of image particles to populate the deficient regions and the use of linear extrapolation to determine the velocity of these image particles from that of fluid particles. A consistent treatment of boundary conditions, utilising the momentum equation to obtain approximations to the velocity of image particles, is described. The method ensures second order approximation of the boundary conditions. It is validated for Poiseuille and Couette flow, for which analytical series solutions exist and shows second order convergence under certain conditions.

1. Introduction

Smoothed particle hydrodynamics (SPH) is a Lagrangian meshless method for obtaining numerical solutions to fluid flow problems [9]. In the SPH framework, the fluid is represented by a collection of particles that are free to move. The system of partial differential equations governing the fluid flow is replaced by equations of motion for these particles. The approach, therefore, is quite distinct from traditional methods in CFD that discretize the governing continuum equations on a fixed grid of points or elements using finite difference, finite element or finite volume approximations.

SPH has a number of advantages and features that make it attractive for use in CFD for certain classes of flow problems in preference to traditional grid-based methods. Since SPH is a fully Lagrangian technique, it is particularly well-suited for convection-dominated problems. Free surface problems and multiphase flows are also easily handled using SPH without the need to explicitly track the interface. The similarity between SPH and molecular dynamics simulation techniques means that it is often possible to incorporate complex physics into the method. Complex geometries can be handled relatively easily using SPH and therefore the method is comparatively straightforward to programme.

Another unique and attractive characteristic of the SPH method is the harmonious combination of the Lagrangian formulation and particle approximation which means that SPH particles not only function as interpolation points, as do particles in other mesh-free methods, but also carry material properties.

Although the SPH method was originally developed for astrophysical applications [4], it has been extended and applied to a wide range of problems in CFD such as free surface [8], multiphase [10], geophysical [12] and viscoelastic flows [3]. In typical astrophysical applications, SPH is used to model compressible fluids at high Reynolds number ($Re \geqslant 10^3$) [1]. On the other hand, the simulation of low Reynolds number incompressible flows required some modification of the original SPH components such as the treatment of viscosity, equation of state, kernel interpolation and boundary conditions. Contributions to these developments were made by Takeda et al. [19] and Morris et al. [11].

The essence of SPH is to choose a smoothing kernel, $W(r,h)$ (h being the smoothing length), and to use it to localise a continuous field through a convolution integral [6]. Such kernels usually possess a compact support radius, R, which is often chosen to be a multiple of the smoothing length, e.g. $R = 2h$. As SPH was developed for use in astrophysics, the satisfaction of boundary conditions was not of immediate concern [15]. However, when the technique was extended to simulate confined flows the implementation and satisfaction of boundary conditions became an issue since the smoothing operation encounters kernel sum deficiencies in the vicinity of solid walls [3]. More precisely, if the normal distance d between the no-slip boundary and the particle position, in

* Corresponding author. Tel.: +44 29 2087 4194; fax: +44 29 2087 4199.
E-mail addresses: BierbrauerF@cardiff.ac.uk (F. Bierbrauer), BolladaPC@cardiff.ac.uk (P.C. Bollada), PhillipsTN@cardiff.ac.uk (T.N. Phillips).

0045-7825/$ - see front matter © 2009 Elsevier B.V. All rights reserved.
doi:10.1016/j.cma.2009.06.014

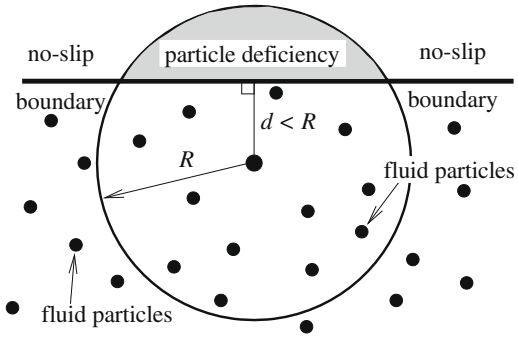

Fig. 1. Diagram showing the deficiency of particles outside a wall boundary for a given compact support radius R.

Fig. 1, at which the interpolation is to be carried out, is less than or equal to the support radius there is insufficient particle information for an accurate calculation. Note that interpolation in SPH is a smoothing operation in which the interpolation of particle values is generally not equal to that of the dependent variable. Therefore, it is simply not enough to set the velocity at boundary positions to zero in order to enforce homogeneous boundary conditions [2]. Difficulties in enforcing the correct boundary conditions allow the growth of errors at the boundary which eventually diffuse into the domain leading to global inaccuracy. It is therefore necessary to ensure boundary conditions are satisfied, at least to the order of accuracy that is present in the method away from the boundaries. Monaghan [9] first proposed replacing the boundary with particles which interact with the fluid through repulsive boundary forces. However, this approach is not simple to implement and, to realistically model low Reynolds number flows, true no-slip boundary conditions are needed [11]. Invariably this led to the use of virtual or image particles which are introduced to overcome the particle deficiency problem at boundaries.

In the approach of Morris et al. [11], the location of image (I) particles remains constant in time with velocities assigned by linear extrapolation from the velocity of fluid (F) particles lying close to the normal drawn between the boundary (W) and the image particle. This is shown in Fig. 2a where the normal projection of the image particle onto the boundary is not coincident with the corresponding normal projection of the fluid particle onto the boundary. In this case we say that the two normal projections

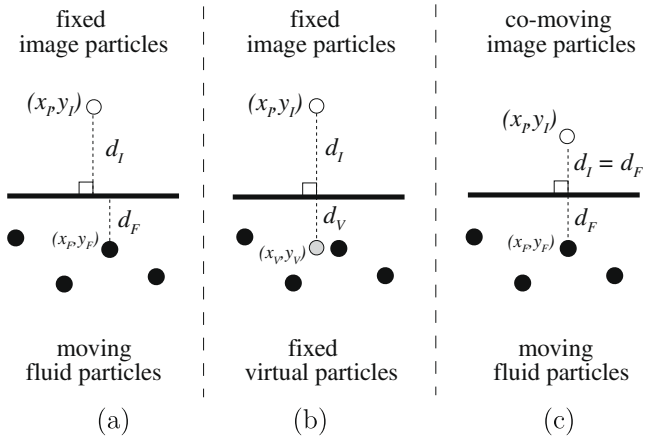

Fig. 2. The assignment of image particle velocities through extrapolation from fluid particles inside the domain using the approach of (a) Morris et al. [11], offset, non-integral reflection using fixed image particles; (b) Fang et al. [3], non-integral reflection using fixed image and fixed virtual particles which are not offset and (c) the approach of the authors: integral reflection using co-moving image particles, also not offset.

are offset. The ratio of the distance between the image particle and the boundary d_I compared to the distance between the fluid particle and the boundary d_F is not necessarily an integer, i.e. $d_I/d_F \neq m$, for m an integer. The method may be summarised as one in which the normal projections of image and fluid particles onto the boundary are offset and d_I/d_F is, in general, non-integral. A linear extrapolation of fluid particle information to image particles uses the weighted average

$$\mathbf{u}_I = \mathbf{u}_F + \left(1 + \frac{d_I}{d_F}\right)(\mathbf{u}_W - \mathbf{u}_F). \tag{1}$$

The extrapolation error introduced by the fact that the normal projections from the image and domain particles onto the boundary are offset is rectified in the work of Fang et al. [3] by creating a set of fixed virtual (V) particles inside the domain so that the normal projections are not offset (see Fig. 2b). These extra virtual particles are assigned velocities through interpolation from surrounding domain particles [3]. In this method d_I/d_V is in general, also non-integral. The extrapolation is given by

$$\mathbf{u}_I = \mathbf{u}_V + \left(1 + \frac{d_I}{d_V}\right)(\mathbf{u}_W - \mathbf{u}_V). \tag{2}$$

Although the approaches based on image particles work and have been used by many researchers they do require extra particles lying outside the domain that extend as far as the support radius in order to obtain the required accuracy. This means that, for large support radii, a large number of image particles are needed. This approach also relies on a weighted averaging which satisfies the boundary conditions, e.g. for the first image particle beyond the boundary when $d_I = d_F : \mathbf{u}_W = (\mathbf{u}_I + \mathbf{u}_F)/2$.

However, it is also possible to correct the kernel estimate in the interpolation by separating particle contributions into those from particles lying in the fluid, particles lying directly on the boundary and those exterior particles needed to alleviate the deficiency of particles near the boundary. Randles and Libersky [15] used this approach without explicitly needing to make use of these exterior particles but simply requiring them to satisfy the kernel estimate of unity. While this approach avoids the need for the creation of extra image particles, it is not clear how accurate this approach is or if it is better than the image particle technique.

In this paper a new approach is advocated which resolves the particle deficiency problem near no-slip boundaries in SPH through a direct application of the Navier–Stokes equations on the boundary without the use of artificial image particles. This method is characterised by an integral extrapolation of particle information to image particles and the normal projection of fluid and associated image particles onto the boundary that are not offset. It is also significantly different from either of the other two approaches in that its image particles are always co-moving with a corresponding fluid particle thereby allowing an exact reflection without recourse to artificial virtual particles. In order to validate this new approach the Poiseuille and Couette flow problems considered by Morris et al. [11] are used as benchmark problems.

In Section 2 the particular SPH model used in this paper is outlined. The algorithmic details follow closely those described in Shao and Lo [17] and Sigalotti et al. [18]. Plane Poiseuille flow in a channel and Couette flow between infinite plates is described including the use of a body force, for Poiseuille flow, to represent the pressure gradient in the flow. In Section 3 the new method is described in detail as well as its accuracy and application to both of the test cases. Section 4 displays the results of simulations for both cases. The influence of the initial particle mesh spacing and smoothing length on the accuracy of the approximation is investigated. This allows the accuracy and order of convergence of the method to be analysed. Section 5 summarises the main findings of the paper.

2. Governing equations and model problems

In smoothed particle hydrodynamics the fluid is represented by particles which follow the fluid motion. Each particle carries mass, velocity and other fluid quantities. The conservation equations governing fluid dynamics are expressed as summation interpolants using an interpolation function W that gives the kernel estimate of the fluid variables at a point. The fluid property at a particle point "a" is evaluated by performing a weighted sum over surrounding particles "b" lying within the support of the kernel

$$W_{ab} = W(r_{ab}, h) = \frac{1}{h^2} g\left(\frac{r_{ab}}{h}\right),$$

where $\mathbf{r}_{ab} = \mathbf{r}_a - \mathbf{r}_b$ and $r_{ab} = |\mathbf{r}_{ab}|$ is the distance between particles located at positions $\mathbf{r}_a = (x_a, y_a)$ and $\mathbf{r}_b = (x_b, y_b)$, and h is the so-called smoothing length defining the support of the interpolation function g. In SPH the interpolation of any function f at position $\mathbf{r}$ is based on the kernel estimate

$$f(\mathbf{r}) \simeq \int f(\mathbf{r}') W(\mathbf{r} - \mathbf{r}', h) d\mathbf{r}', \tag{3}$$

where $d\mathbf{r}'$ is a volume and where the delta function in the identity $f(\mathbf{r}) = \int f(\mathbf{r}')\delta(\mathbf{r} - \mathbf{r}')d\mathbf{r}'$ has been replaced by a kernel function $W(\mathbf{r} - \mathbf{r}', h)$. Such an estimate is a good one provided that the kernel function reduces to the delta function when $\lim_{h\to 0} W(\mathbf{r} - \mathbf{r}', h) = \delta(\mathbf{r} - \mathbf{r}')$, is normalised such that $\int W(\mathbf{r}, h)d\mathbf{r} = 1$ and has compact support on a disk $D = \{\mathbf{r} : |\mathbf{r}| < R\}$, i.e. $W(\mathbf{r}, h) = 0$ for $\mathbf{r} \in \overline{D} = I\!R^2 \setminus D$. The continuous volume integral (3) may be approximated by a finite sum over discrete interpolation points, or 'particles', so that for any volume integral $\int \phi(\mathbf{r}')d\mathbf{r}' \simeq \sum_{b=1}^{N} \frac{\phi(\mathbf{r}_b)}{\rho_b} m_b$ where the volume $d\mathbf{r}' = m/\rho$ and m_b is interpreted as the mass associated with an interpolation point b and we have summed over N interpolation points. This means that any scalar variable f at particle position $\mathbf{r}_a$, may be approximated by:

$$f(\mathbf{r}_a) = \sum_{b=1}^{N} \left(\frac{m_b}{\rho_b}\right) f(\mathbf{r}_b) W(\mathbf{r}_a - \mathbf{r}_b, h), \tag{4}$$

where N is the total number of particles.

In a two dimensional domain of dimension $L \times H$, the constant average particle volume V_0 is given by $V_0 = LH/N$, i.e. the total domain area is distributed equally to each particle. The mass of particle b is then given by $m_b = \rho_b V_b = \rho_b V_0$. In this paper we mainly use the approach of Morris et al. [11], with some modifications, to discretise the various conservation equations.

The Navier–Stokes equations in SPH form are those used in [17]. Throughout, we have scaled them with respect to length L, velocity U_0, time L/U_0, density ρ_0, viscosity μ_0 and pressure $\rho_0 U_0^2$. Particle density is evolved with the non-dimensional SPH equation for continuity [11]:

$$\frac{D\rho_a}{Dt} = \frac{H}{LN} \sum_{b=1}^{N} \rho_b \mathbf{u}_{ab} \cdot \nabla_a W_{ab} \tag{5}$$

and the gradient is evaluated with respect to the coordinates of particle a. One way to model incompressible flow in SPH is to use an artificial quasi-incompressible equation of state with a sound speed low enough to be practical and also high enough to maintain an approximately constant density at each time step. At low Reynolds numbers more accurate pressure estimates are obtained, as well as eliminating numerical instabilities in regions of low pressure, when the non-dimensionalised equation of state

$$p = \frac{1}{M^2}\rho \tag{6}$$

is used [11]. The sound speed must be chosen to be large enough so that the behaviour of the quasi-incompressible fluid is close to that of the real fluid while not being so large that the time step becomes prohibitively small [11]. In this paper the sound speed is chosen as $c = 10U_0$ giving a Mach number $M = 0.1$, where U_0 is the characteristic velocity. The non-dimensional momentum equation at particle a may then be written as

$$\frac{D\mathbf{u}_a}{Dt} = -\left(\frac{H}{L}\right)\frac{1}{Re}\frac{1}{N}\sum_{b=1}^{N} \rho_b \left(\frac{p_a}{\rho_a^2} + \frac{p_b}{\rho_b^2} + \chi_{ab}\right)\nabla_a W_{ab} + \mathbf{F}_a. \tag{7}$$

The pressure gradient term is designed to conserve total linear and angular momentum. The viscous stresses for incompressible flows used by Shao and Lo [17] is implemented

$$\chi_{ab} = -\left(\frac{4(\mu_a + \mu_b)}{(\rho_a + \rho_b)^2}\right)\frac{\mathbf{u}_{ab} \cdot \mathbf{r}_{ab}}{|\mathbf{r}_{ab}|^2}. \tag{8}$$

For the case of constant density, which is the situation considered in this paper, this expression is the same as that used by Morris et al. [11]. Here, $\mathbf{F}_a$ represents the known non-dimensionalised external force such as gravity or other body forces.

In this paper we use the cubic spline kernel which has compact support, the second derivative is continuous with a dominant error in the integral interpolant of $O(h^2)$ making the kernel insensitive to particle disorder [7]. This is defined through the interpolation function g mentioned previously and given by:

$$g(s) = \frac{10}{7\pi}\begin{cases} 1 - 3s^2/2 + 3s^3/4, & 0 \leqslant s < 1, \\ (2-s)^3/4, & 1 \leqslant s < 2, \\ 0, & s \geqslant 2. \end{cases} \tag{9}$$

This choice of kernel ensures that the support radius is $R = 2h$.

All computations are performed within a non-dimensionalised domain defined by $0 \leqslant x \leqslant 1$ and $0 \leqslant y \leqslant H/L$. The initial particle configuration is a rectangular lattice defined by

$$x_a = i\Delta x \quad \text{for } i = \{1, I\},$$
$$y_a = (j-1)\Delta y \quad \text{for } j = \{1, J+1\},$$

where $\Delta x = 1/I, \Delta y = H/(LJ)$. Note that there are only I particles in the x direction whereas there are $J+1$ in the y direction. Due to the use of periodic boundary conditions at $x = 0, 1$ particles leaving the right-hand side boundary at $x = 1$ re-enter the left-hand side at $x = 0$ which can result in an excess number of particles there leading to an incorrect interpolation. This makes a total number of $N = I(J+1)$ fluid particles in the domain and on the boundaries. Note that this initial regular configuration will change to a more irregular one as the flow progresses in time.

We use a modified predictor–corrector scheme, with improved stability properties, to solve the equations of motion and the particle update equation $d\mathbf{r}_a/dt = \mathbf{u}_a$ as detailed in [13] with a predictor step given by

$$\mathbf{u}^{n+1/2} = \mathbf{u}^n + \frac{\Delta t}{2}\mathsf{F}^n, \quad \mathbf{r}^{n+1/2} = \mathbf{r}^n + \frac{\Delta t}{2}\mathbf{u}^{n+1/2},$$
$$\rho^{n+1/2} = \rho^n + \frac{\Delta t}{2}\mathsf{M}^n,$$

where $\mathsf{F}^{n+1/2} = \mathsf{F}(\mathbf{r}^{n+1/2}, \mathbf{u}^{n+1/2}), \mathsf{M}^{n+1/2} = \mathsf{M}(\rho^{n+1/2}, \mathbf{u}^{n+1/2})$ represent the forces and mass flux in the flow (we use different fonts to differentiate between the body force F and total forces F = pressure + viscous + body forces, and mass m and mass flux $\mathsf{M} = -\rho\nabla \cdot \mathbf{u}$). The corrector step is then

$$\mathbf{u}^* = \mathbf{u}^n + \frac{\Delta t}{2}\mathsf{F}^{n+1/2}, \quad \mathbf{r}^* = \mathbf{r}^n + \frac{\Delta t}{2}\mathbf{u}^*, \quad \rho^* = \rho^n + \frac{\Delta t}{2}\mathsf{M}^{n+1/2}$$

followed by

$$\mathbf{u}^{n+1} = 2\mathbf{u}^* - \mathbf{u}^n, \quad \mathbf{r}^{n+1} = 2\mathbf{r}^* - \mathbf{r}^n, \quad \rho^{n+1/2} = 2\rho^* - \rho^n$$

The non-dimensionalised stability requirements [11] are: the CFL condition, $\Delta t \leqslant hM/4$, viscous diffusion, $\Delta t \leqslant Reh^2/8$, and the constraint due to the magnitude of particle accelerations $\Delta t \leqslant \min_a \sqrt{Reh/|\mathrm{F_a}|}$.

2.1. Exact solutions

Two well known exact solutions to the incompressible Navier–Stokes equations have been chosen as test cases: Poiseuille (P) and Couette (C) flow. For Poiseuille flow we consider unsteady flow between two infinite parallel plates, located at $y = 0, H/L$, at rest in the presence of a pressure gradient. We follow Sigalotti et al. [18] in defining a dynamic pressure p such that $p = p_T - p_H$ where p_T is the total pressure and p_H is the hydrostatic pressure. The hydrostatic pressure is here used as a body force $\mathbf{F} = (F^x, F^y) = -\nabla p_H/\rho = (8\mu U_0/\rho H^2, 0)$ acting throughout the domain. The exact non-dimensional solution for the horizontal velocity component may then be expressed as

$$\mathrm{u}_P(x,y,t) = -\left(\frac{2L}{H}\right)^2 y(y - H/L) - \sum_{n=0}^{\infty} \frac{32}{\pi^3(2n+1)^3} \times \sin\left[\frac{(2n+1)\pi y}{H/L}\right] \exp\left[-\frac{(2n+1)^2\pi^2 t}{Re\rho(H/L)^2}\right]. \tag{10}$$

The flow is then driven by an applied body force $F^x = 8\mu U_0/\rho H^2$ here given through the hydrostatic pressure gradient. Initially, all particle velocities within the domain are chosen to be zero, $\mathbf{u}_a^0 = \mathbf{0}$, with constant density, $\rho_a^0 = 1$, viscosity, $\mu_a^0 = 1$, as well as volume $V_a = V_0$. Velocity boundary conditions are no-slip at the top and bottom boundaries, $\mathbf{u}(x, 0; H/L, t) = \mathbf{0}$, and periodic along the left and right boundaries, $\mathbf{u}(0, y, t) = \mathbf{u}(1, y, t)$. Boundary conditions on the density and viscosity are homogeneous Neumann at the top and bottom and periodic at the left and right boundaries.

The Couette flow case is similarly defined between two parallel plates located at $y = 0$ and $y = H/L$. Again, the system is initially at rest with the same fluid properties as for the Poiseuille flow case above. The only difference in initial and boundary conditions from the Poiseuille flow case is that the upper plate moves with a constant velocity $u(x, H/L, t) = 1$ and $\mathbf{F} = \mathbf{0}$ which applies for $t \geqslant 0$. The exact solution is given by:

$$\mathrm{u}_C(x,y,t) = \frac{Ly}{H} + \sum_{n=1}^{\infty} \frac{2}{n\pi}(-1)^n \sin\left(\frac{nL\pi y}{H}\right) \exp\left(-\frac{n^2\pi^2 t}{Re\rho(H/L)^2}\right). \tag{11}$$

We chose to use the specifications of the problem studied in Morris et al. [11] with the characteristic parameters given by $\rho_0 = 1000\ \mathrm{kg\ m^{-3}}$, $\mu_0 = 0.001\ \mathrm{kg\ m^{-1}s^{-1}}$, $U_0 = 1.25 \times 10^{-5}\ \mathrm{m\ s^{-1}}$, $L = H = 0.001\ \mathrm{m}$, $c = 10U_0$ so that $Re = \rho_0 U_0 L/\mu_0 = 0.0125$ and $M = U_0/c = 0.1$, a subsonic Mach number considered to be a good approximation to the incompressibility constraint [18].

3. Consistent boundary conditions

The evaluation of boundary conditions in SPH, for the present set of problems, involves no-slip boundaries on the top and bottom boundaries, periodic boundaries at the left and right boundaries and a combination of the two near boundary corners.

3.1. Periodic boundaries

The two test problems both make use of periodic boundary conditions at $x = 0, 1$. Periodic boundaries are actually just the continuation of the domain from one side into the other. Then, for any scalar variable $f(x, y, t)$ at periodic boundaries we have $f(0, y, t) = f(1, y, t)$. It also means that any interpolation circle overlapping one of the periodic boundaries automatically overlaps the other as well. Consider the right boundary at $x = 1$. Any interpolation for a particle within the support length of this boundary will overlap the boundary and also appear to the right of the left boundary at $x = 0$. This means that if the interpolation circle was originally centred on a particle (x_a, y_a), where $1 - x_a < R$, its partner circle to the left of the left boundary must be centred at $(x_a - 1, y_a)$. A typical update of the form (4) may be constructed by taking into account information from the right and left boundaries, that is

$$f(\mathbf{r}_a) = \frac{H}{LN}\left(\sum_{\mathbf{r}_b \in \overline{\Omega}_R} f(\mathbf{r}_b) W(\mathbf{r}_a - \mathbf{r}_b, h) + \sum_{\mathbf{r}_b \in \Omega_L} f(\mathbf{r}_b) W(\mathbf{r}_{a'} - \mathbf{r}_b, h)\right),$$

where $\Omega_R = \{(x,y) : (x - x_a)^2 + (y - y_a)^2 \leqslant (R/L)^2, x < 1\}$, $\overline{\Omega}_R = \{(x,y) : (x - x_a)^2 + (y - y_a)^2 \leqslant (R/L)^2, x \leqslant 1\}$ and $\Omega_L = \{(x,y) : (x - x_a)^2 + (y - y_a)^2 \leqslant (R/L)^2, x > 0\}$. Any particle lying on the boundary at $x = 1$ is included through the sum over the region $\overline{\Omega}_R$. The update for f_a now reads

$$f_a = \frac{H}{LN}\left(\sum_{b=1}^{N} f_b W_{ab} + \sum_{b=1, x_b \neq 0}^{N} f_b W_{a'b}\right),$$

where $(x_{a'}, y_{a'}) = (x_a - 1, y_a)$. Note that any fluid variable involving information at (x_a, y_a) such as the pressure p_a or velocity $\mathbf{u}_a$ retains its value in the corresponding interpolation circle at the opposite boundary. This remains true of the density, viscosity and distance $r_{a'b}$ so that $\chi_{a'b} = \chi_{ab}$.

The update of the momentum equation, for both the Poiseuille and Couette flow cases, near the right boundary $x = 1$, where $(x_{a'}, y_{a'}) = (x_a - 1, y_a)$, becomes

$$\mathbf{u}_a^{n+1} = \mathbf{u}_a^n - \left(\frac{H}{LN}\right)\frac{\Delta t}{Re}\left[\sum_{b=1}^{N} \rho_b(p_{ab} + \chi_{ab})\nabla_a W_{ab} + \sum_{b=1, x_b \neq 0}^{N} \rho_b(p_{ab} + \chi_{ab})\nabla_{a'} W_{a'b} + \mathbf{F}_a\right],$$

where $p_{ab} = p_a/\rho_a^2 + p_b/\rho_b^2$ and $F_C^x = F_{P,C}^y = 0$ and $F_P^x = 8L^2/H^2$. The update of the continuity equations becomes

$$\rho_a^{n+1} = \rho_a^n + \left(\frac{H\Delta t}{LN}\right)\left(\sum_{b=1}^{N} \rho_b \mathbf{u}_{ab} \cdot \nabla_a W_{ab} + \sum_{b=1, x_b \neq 0}^{N} \rho_b \mathbf{u}_{ab} \cdot \nabla_{a'} W_{a'b}\right).$$

The update for particles lying near the left boundary is similar with the only exception being that the corresponding interpolation circle is now centred at $(x_a + 1, y_a)$.

3.2. No-slip boundaries

The essence of the current idea is to resolve the particle deficiency problem near boundaries by approximating the velocity at exterior image particles through a second order finite difference approximation of the Navier–Stokes equations on the boundary itself, specifically the momentum equation. This allows the new method to be an integral reflection while not being offset as shown in Fig. 2c. The two-step process involves (i) exactly reflecting image particle positions with regard to domain particle locations, thus each image particle is a partner of a corresponding fluid particle and (ii) using the Navier–Stokes equations to approximate image particle velocities.

Consider a no-slip (wall) boundary along the boundary line $y = H/L$, as shown in Fig. 3 with velocity condition $\mathbf{u}_W = \mathbf{u}(x, H/L, t)$. We assign any scalar quantity such as density for the image particle to be the same as that of its corresponding fluid

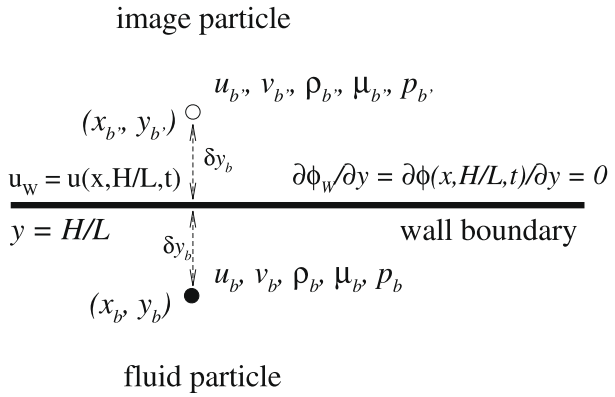

Fig. 3. Fluid particle b, and image particle b', on either side of a wall boundary, with velocity $\mathbf{u}_W = \mathbf{u}(x, H/L, t)$, with corresponding velocities, densities, viscosities, pressures and Neumann conditions on scalar fields $\phi = \{\rho, \mu, p\}$.

particle which is akin to that of the imposition of a Neumann condition as used by [13,17], i.e. for scalar $\phi = \{\rho, \mu, p\}$, so that $\partial\phi(x, H/L, t)/\partial y = 0$. Therefore particles lying on the boundary possess the wall velocity condition. However, the density, viscosity and pressure of these particles are not as easily evaluated since only a Neumann condition is specified on this boundary. These conditions are shown in Fig. 3. For particles lying inside the fluid but 'near enough' to the boundary (this will be explained shortly) at (x_b, y_b), and a normal distance $\delta y_b = H/L - y_b$ from the boundary line, it is possible to construct a partner image particle beyond the boundary the same normal distance from the boundary, that is at $(x_{b'}, y_{b'}) = (x_b, H/L + \delta y_b)$. A simple second order finite difference approximation of the Neumann conditions gives $\rho_{b'} = \rho_b, \mu_{b'} = \mu_b$ and $p_{b'} = p_b$. It is also possible to obtain an expression for the image particle velocity using the given wall condition but this is only an average of low order accuracy. Instead, we will make use of the Navier–Stokes equations at the boundary to evaluate the velocity at the exterior image particle position. At any given time the velocity field already obeys the mass conservation equation but the momentum equations are explicitly given at the boundary as:

$$(\mathbf{u}_t + (\mathbf{u}\cdot\nabla\mathbf{u}))_W = \frac{1}{Re}\left(-\frac{1}{\rho}\nabla p + \frac{1}{\rho}\nabla^2\mathbf{u} + \frac{1}{\rho}\mathbf{F}\right)_W. \tag{12}$$

Now, the time derivative of the velocity condition $\mathbf{u}_t(x, H/L, t)$ may be explicitly calculated as well as the derivatives $\mathbf{u}_x, \mathbf{u}_{xx}$. The only terms not explicitly defined are p_x, and all y derivatives of the velocity which, however, may be approximated using a second order centred finite difference approximation (see Fig. 3):

$$(\mathbf{u}_{yy})_W \simeq \frac{\mathbf{u}_{b'} - 2\mathbf{u}_W + \mathbf{u}_b}{\delta y_b^2} + O(\delta y_b^2).$$

The momentum equation (12) may then be used to express the image particle velocities as

$$\begin{aligned}\mathbf{u}_{b'} = {} & \left[2\left(\frac{2}{2 - Re\rho_W v_W \delta y_b}\right)\mathbf{u}_W - \left(\frac{2 + Re\rho_W v_W \delta y_b}{2 - Re\rho_W v_W \delta y_b}\right)\mathbf{u}_b \right.\\ & + \left(\frac{2Re\rho_W \delta y_b^2}{2 - Re\rho_W v_W \delta y_b}\right)\left((\mathbf{u}_t)_W + (\mathbf{u}_x)_W + \frac{(\nabla p)_W}{Re\rho_W}\right.\\ & \left.\left. - \frac{1}{Re\rho_W}(\mathbf{u}_{xx})_W - \frac{1}{Re\rho_W}\mathbf{F}_W\right)\right].\end{aligned} \tag{13}$$

It is clear that this expression is completely general and takes into account the presence of any body force terms whether this is represented by the pressure gradient force term in Poiseuille flow or additional forces such as gravity. When the velocity boundary condition is a constant, $\mathbf{u}_W = (1, 0)$ for the Poiseuille case and $\mathbf{u}_W = \mathbf{0}$ for the Couette case we obtain

$$\mathbf{u}_{b'} = 2\mathbf{u}_W - \mathbf{u}_b + \delta y_b^2((\nabla p)_W - \mathbf{F}_W) \tag{14}$$

plus terms of order $O(\delta y_b^4)$. Eq. (14) clearly shows that the usual averaging extrapolation in common use is second order accurate in δy_b whereas the approach used above is automatically fourth order accurate provided δy_b remains 'small'. When the particle lies on the boundary $\delta y_b = \delta y_W = 0$ and $\mathbf{u}_{b'} = \mathbf{u}_W$ satisfying the boundary condition exactly.

Note that the condition (13) is calculated at time $t^n = n\Delta t$ where the values $\mathbf{u}_W^n, \rho_W^n, \mu_W^n$ and p_W^n are known. However, the pressure gradient in the x direction is not known. It must be calculated and may be obtained through the use of a centred difference approximation, for example: $(p_x)_W = (p_{a'} - p_a)/(\delta x_{a'b} + \delta x_{ab})$, where $p_a = p(x_a, H/L, t), p_{a'} = p(x_{a'}, H/L, t), \delta x_{a'b} = x_{a'} - x_b$ and $\delta x_{ab} = x_a - x_b$. This involves the location of boundary particles, $(x_a, H/L), (x_{a'}, H/L)$ closest to and on either side of the boundary point $(x_b, H/L)$ so that the distances $\delta x_{a'b}$ and δx_{ab} are, in general, not equal. This means that such an approximation can be at most first order accurate in $\delta x_{a'b} - \delta x_{ab}$. This is not a serious problem as the pressure derivative will always be small in an incompressible flow. The calculations at the $x = 0, 1$ boundaries are obtained from the application of periodic conditions already defined in Section 3.1.

While a simple average, $d_I = d_F$ in (1), of the fluid and image particle velocities satisfies the velocity boundary condition exactly the current method only satisfies the boundary condition up to second order in δy_b. However, the purpose of the method is to accurately approximate the solution beyond the boundary so that it can be used within an interpolation circle which overlaps the boundary to accurately update the Navier–Stokes equations. For example, for Poiseuille flow at steady state, the method obeys the analytical results exactly, i.e. $u_{b'} = u_P(H/L + \delta y_b)$ whereas a simple average is in error by $8L^2\delta y_b^2/H^2$. This means that a simple average will overestimate the solution by this amount.

In addition, it should be noted that, whereas the initial particle spacing Δy tends to remain small, the distance $\delta y_b = H/L - y_b$ may be as large as the non-dimensionalised support radius R/L which is always a multiple of the smoothing length. For simulations using a small number of particles per dimension this radius can be a significant fraction of the domain length/width. This means we require the second order correction term $\delta y_b^2((p_x)_W - 8L^2/H^2)$ to be a local one otherwise higher order terms will be needed. It is easily shown that this remains true as long as $\delta y_b \leqslant H/(2L\sqrt{2 - Re})$ and $\delta y_b \leqslant H/(2L\sqrt{Re})$, for the Poiseuille and Couette flow cases, respectively.

Similarly, since the normal distance δy_b may be as large as the support radius the same criterion limits the support radius. Then, since $R/L = 2h$ and the smoothing length is always some real multiple of the initial inter-particle spacing $h = q\Delta y$ and using the fact that $H/L = J\Delta y$, the support radius inequality allows the construction of the maximum allowable multiple q as $q_P \leqslant J/(4L\sqrt{2 - Re})$ and $q_C \leqslant J/(4L\sqrt{Re})$. For a set number of particles per dimension, in the present case $J = \{16, 24, 32, 48, 64\}$, we expect $q_P \leqslant \{1.9, 2.8, 3.8, 5.7, 7.6\}$ and $q_C \leqslant \{23.8, 35.8, 47.8, 71.5, 95.4\}$ for the Poiseuille and Couette flow cases respectively. This implies that a choice of $q_P = 3$, in the Poiseuille flow case when $J = 16$, could produce larger errors than intended whereas this cannot occur in the Couette flow case as q_C always exceeds even the lowest expected values that can be obtained from $J/4L\sqrt{Re}$ using the present grid sizes and support radii.

3.2.1. Incorporation into the Navier–Stokes equations

Before incorporating the new boundary condition approach into the update of the Navier–Stokes equations, it is important to note that only those particles lying within the support radius of a no-slip boundary possess an interpolation circle which may overlap

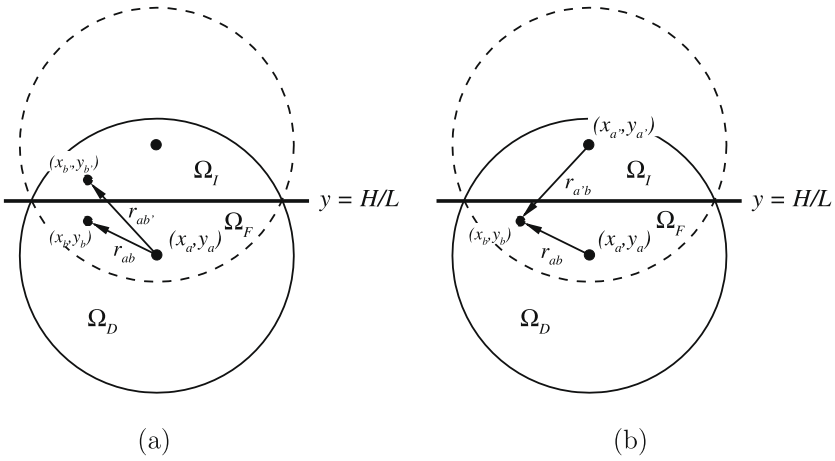

Fig. 4. (a) Boundary overlap of an interpolation circle centred at (x_a, y_a) and definition of domain Ω_D and image particle regions Ω_I, (b) construction of image circle centred at $(x_{a'}, y_{a'}) = (x_a, 2H/L - y_a)$.

the boundary. Any interpolation of a scalar function such as (4), where the interpolation region overlaps the boundary, must be separated into contributions from the region within the domain, on the boundary, and the region outside the boundary. For the case of a no-slip wall at $y = H/L$ we get

$$f(\mathbf{r}_a) = \frac{H}{LN}\left(\sum_{\mathbf{r}_b\in\overline{\Omega}_D} f(\mathbf{r}_b)W(\mathbf{r}_a-\mathbf{r}_b,h) + \sum_{\mathbf{r}_{b'}\in\Omega_I} f(\mathbf{r}_{b'})W(\mathbf{r}_a-\mathbf{r}_{b'},h)\right), \tag{15}$$

where $\Omega_D = \{(x,y) : (x-x_a)^2 + (y-y_a)^2 \leqslant (R/L)^2, y < H/L\}$ is the region for those particles inside the domain, $\overline{\Omega}_D = \{(x,y) : (x-x_a)^2 + (y-y_a)^2 \leqslant (R/L)^2, y \leqslant H/L\}$ includes the boundary as well and $\Omega_I = \{(x,y) : (x-x_a)^2 + (y-y_a)^2 \leqslant (R/L)^2, y > H/L\}$ is the region containing image particles outside the domain (see Fig. 4(a)). From Fig. 4(a) it is clear that only those fluid particles, indicated by (x_b, y_b), lying within the region $\Omega_F = \{(x,y) : (x-x_a)^2 + (y-y_a)^2 \leqslant (R/L)^2, y < H/L\}$ require a corresponding image particle, indicated by $(x_{b'}, y_{b'}) \in \Omega_I$. This means that the second sum in (15) may be rewritten in terms of a sum over those fluid particles as 'seen' from the centre of the image circle centred at $(x_{a'}, y_{a'}) = (x_a, 2H/L - y_a)$, but carrying with them the changes made to a particular variable across the boundary, that is

$$\begin{aligned} f(\mathbf{r}_a) &= \frac{H}{LN}\left(\sum_{\mathbf{r}_b\in\overline{\Omega}_D} f(\mathbf{r}_b)W(\mathbf{r}_a-\mathbf{r}_b,h) + \sum_{\mathbf{r}_b\in\Omega_D} \tilde{f}(\mathbf{r}_b)W(\mathbf{r}_{a'}-\mathbf{r}_b,h)\right) \\ &= \frac{H}{LN}\left(\sum_{b=1}^{N} f_b W_{ab} + \sum_{b=1, y_b\neq H}^{N} \tilde{f}_b W_{a'b}\right), \end{aligned} \tag{16}$$

where $\tilde{f}_b$ indicates the change in f_b across the boundary, for example, when $f = u$ we have, for Poiseuille flow, $\tilde{u}_b = -u_b + \delta y_b^2((p_x)_W - 8L^2/H^2)$, whereas if $f = p$ we have $\tilde{p}_b = p_b$.[1] Similarly, any fluid variable evaluated at a retains its value i.e. $p_{a'} = p_a, \mathbf{u}_{a'} = \mathbf{u}_a$. This must be the case as all calculations were originally oriented with regard to particle values inside the fluid. This is shown in Fig. 4b. This simplifies the original calculation as this required non-existent image particles as part of the second sum. In addition, it eliminates the need for another set of image particles outside the domain, now the sums are carried out only over fluid particles within, and on the boundary, of the domain. A similar update is required for the $y = 0$ boundary except that the corresponding image circle is centred at $(x_{a'}, y_{a'}) = (x_a, -y_a)$.

The velocity update, for the Poiseuille and Couette flow cases, within the momentum equations now reads

$$\begin{aligned} \mathbf{u}_a^{n+1} = \mathbf{u}_a^n + \frac{H\Delta t}{ReLN}\Bigg[&\sum_{b=1}^{N} \rho_b(p_{ab} + \chi_{ab})\nabla_a W_{ab} \\ &+ \sum_{b=1, y_b\neq H}^{N} \rho_b(p_{ab} + \chi_{a'b})\nabla_a W_{a'b} + \mathbf{F}_a\Bigg], \end{aligned} \tag{17}$$

where the pressure gradient in the y direction and the position vectors are defined by $(p_y)_W = 0, \mathbf{r}_{ab} = \mathbf{r}_a - \mathbf{r}_b$ and $\mathbf{r}_{a'b} = \mathbf{r}_{a'} - \mathbf{r}_b$. The viscous term (8) includes the velocity difference

$$\mathbf{u}_{ab} = \mathbf{u}_a - 2\mathbf{u}_W + \mathbf{u}_b, \quad \mathbf{u}_{a'b} = \mathbf{u}_{ab} - \delta y_b^2((\nabla p)_W - \mathbf{F}_W),$$

where $\mathbf{u}_W = (1,0)$ for the Poiseuille and $\mathbf{u}_W = \mathbf{0}$ for the Couette flow cases. Note that the update for the velocity vector is performed up to the boundary but the value for $\mathbf{u}_a = \mathbf{u}_W$ is not necessary as this is already known. Similarly, the update of the continuity equation becomes

$$\rho_a^{n+1} = \rho_a^n + \frac{H\Delta t}{LN}\left\{\sum_{b=1}^{N} \rho_b \mathbf{u}_{ab}\cdot\nabla_a W_{ab} + \sum_{b=1, y_b\neq H}^{N} \rho_b \mathbf{u}_{a'b}\cdot\nabla_{a'} W_{a'b}\right\}. \tag{18}$$

3.3. Corner boundaries

At boundary corners an interpolation circle encounters both a periodic and a no-slip condition. The choice of boundary condition in each case depends on the vicinity of the fluid particle to the corner. For example, Fig. 5 shows the top right-hand corner. If the particle is located in region A, defined by $[R/L, 1-R/L]\times((H-R)/L, H/L]$, the update obeys the no-slip condition which has been described in Section 3.2. If the particle lies within region D, defined by $(1-R/L, 1]\times[R/L, (H-R)/L]$, the update follows the procedure described for purely periodic boundary conditions of Section 3.1. If the particle is located within region C, defined by the intersection of the lines $x > 1-R/L, y > (H-R)/L$ and the exterior of the circle $(x-1)^2 + (y-H/L)^2 \geqslant (R/L)^2$, the

[1] The Neumann conditions for the pressure and density indicate that $p_{b'} = p_b$ and $\rho_{b'} = \rho_b$ or $\tilde{p}_b = p_b$ and $\tilde{\rho}_b = \rho_b$. The volume and viscosity remain constant throughout and are also the same $V_{b'} = V_b = V_0, \mu_{b'} = \mu_b = \mu_0$, or $\tilde{V}_b = V_b$ and $\tilde{\mu}_b = \mu_b$.

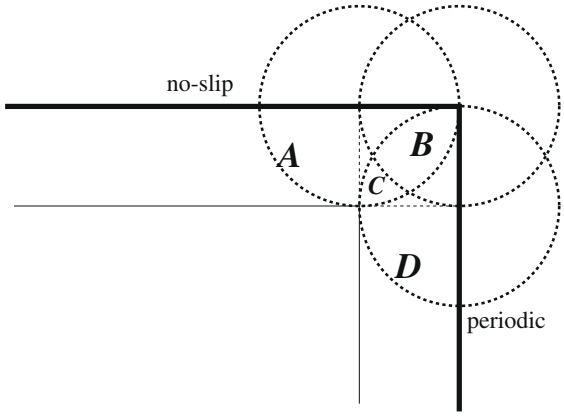

Fig. 5. Evaluation of boundary conditions at a no-slip-periodic corner indicated by four separate regions A, B, C and D.

interpolation circle will only overlap on the top and right boundaries but not at the corner itself. If the particle is located within region B, defined by the curves $x \leqslant 1, y \leqslant H/L$ and $(x-1)^2 + (y - H/L)^2 < (R/L)^2$, then the interpolation circle overlaps at all boundaries including at the corner itself. A similar set of criteria are required at the remaining corners.

In region C the inclusion of boundary conditions follows what was done previously for the periodic and no-slip approaches except that the original interpolation is now separated into three instead of two sums. For a scalar function f_a:

$$f_a = \frac{H}{LN}\left(\sum_{b=1}^{N} f_b W(x_{ab}, y_{ab}) + \sum_{b=1, y_b \neq H}^{N} f_b^T W(x_{ab}, y_{ab}^T) + \sum_{b=1, x_b \neq L}^{N} f_b W(x_{ab}^R, y_{ab})\right), \tag{19}$$

where $x_{ab}^R = x_a - 1 - x_b$ indicates the right (R) boundary, $y_{ab}^T = 2H/L - y_a - y_b$ indicates the top (T) boundary so that $r_{ab}^T = \sqrt{(x_{ab})^2 + (y_{ab}^T)^2}$ and $r_{ab}^R = \sqrt{(x_{ab}^R)^2 + (y_{ab})^2}$. Here, f^T indicates the changes in f across the top no-slip boundary whereas there are no changes for the periodic boundaries. The approach of dividing the original sum in region C into three separate sums, as shown in (19), may be used to update the momentum and continuity equations for the Poiseuille and Couette flow cases in an analogous way as was done in Section 3.2.1. A similar set of updates are required for the top-left, bottom-left and bottom-right corners with corresponding image circle centres.

In region B, the top-right (TR) corner, the interpolation now includes four separate sums given by

$$f_a = \frac{H}{LN}\left(\sum_{b=1}^{N} f_b W(x_{ab}, y_{ab}) + \sum_{b=1, y_b \neq H}^{N} f_b^T W(x_{ab}, y_{ab}^T) + \sum_{b=1, x_b \neq L}^{N} f_b W(x_{ab}^R, y_{ab}) + \sum_{b=1, x_b \neq L, y_b \neq H}^{N} f_b^T W(x_{ab}^R, y_{ab}^T)\right), \tag{20}$$

so that an analogous inter-particle distance $r_{ab}^{TR} = \sqrt{(x_{ab}^R)^2 + (y_{ab}^T)^2}$. Note that the corresponding change in f is given by f^T rather than f^{TR} as there is no change across the periodic boundary. The same procedure (20) may again be used to update the momentum and continuity equations for the two flow cases. A similar set of updates are needed for the top-left, bottom-left and bottom-right corners in addition to their corresponding image circle centres.

4. Numerical results and discussion

SPH possesses two distinct length scales: the average inter-particle spacing Δx which corresponds approximately to $1/n$, the inverse of the number of particles per dimension, and the smoothing length h [5], rather than one as for example with finite difference methods which only require Δx. Quinlan et al. [14] have shown that the discrete convergence characteristics of SPH depend on both the smoothing error, which is a function of smoothing length h, and the discretisation error, which depends on the ratio of smoothing length to inter-particle spacing, $h/\Delta x$. This means that as $h/\Delta x$ is increased, accuracy becomes limited by smoothing error. However as the smoothing length decreases, the error becomes dominated by discretisation error. Second order accuracy in h is possible when smoothing error dominates so that $h/\Delta x$ is large [14]. These two independent parameters are equivalent to saying that higher order accuracy is obtained when both the number of particles n in the simulation and the number of particle neighbours per dimension $n_n \simeq 2h/\Delta x$ are increased with n increasing faster than n_n otherwise the method is inconsistent [16].

In both the Poiseuille and Couette flow problems the algorithm was run up to the steady state which is considered to be fully developed at approximately $t = 1$ s [5] which corresponds to a non-dimensional time T = 0.0125. In the two test cases the initial particle configuration was a regular lattice as described in Section 2. However, since $\Delta x = \Delta y$ we make use only of Δx to indicate the initial inter-particle spacing. As such, the solution may be analysed by considering this initial lattice as a 'grid'. In this paper we chose to use the following grids: $16^2, 24^2, 32^2, 48^2, 64^2$. Given the small Reynolds number used particle motion is limited for this timescale so that an assumption using Δx as the average inter-particle spacing remains approximately valid. In the following numerical convergence is studied by plotting how the error varies with the smoothing length h and the number of particles $n = 1/\Delta x$ so that we may make a comparison with the results of Graham and Hughes [5] and Quinlan et al. [14].

4.1. Post-processing

4.1.1. 2D slice

Typically, the accuracy of the solution is studied by taking a plane slice through the three dimensional data (x, y, u) at $x = 1/2$ for the horizontal velocity $u(1/2, y, t)$. Although the actual data points will not necessarily lie on the chosen plane the velocity information there can be obtained by perpendicularly projecting the velocity data from those points (x_p, y_p) lying closest to the plane $x = 1/2$ (see Fig. 6). Given that these points will generally lie within the inter-particle distance Δx there is little inaccuracy in this approach.

4.1.2. Errors

Although taking a slice of the 2D horizontal velocity information allows a qualitative comparison with the analytical results, it introduces some extra error. This is avoided if a direct error analysis is made by using the velocity data already obtained from numerical calculations, i.e. the set of data $\mathbf{u}_n(\mathbf{r}_b, t^n)$, which allows a direct comparison with analytical results $\mathbf{u}_e(\mathbf{r}_b, t^n)$, where e and n refers to the exact and numerical data respectively. The L_2 error $E = \|\mathbf{u}_e - \mathbf{u}_n\|_2$ is then obtained as follows:

$$\|\mathbf{u}_e - \mathbf{u}_n\|_2 = \left(\frac{1}{N}\sum_{b=1}^{N} |\mathbf{u}_e(\mathbf{r}_b, t) - \mathbf{u}_n(\mathbf{r}_b, t)|^2\right)^{1/2}, \tag{21}$$

where we have summed over all N particles b and averaged the result. The order of the error may be analysed by assuming its size to be a power of smoothing length, h, so that $E(h) \propto h^p$. A comparison

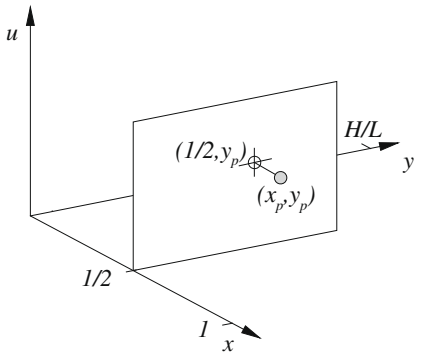

Fig. 6. Projection of particle velocity data u_p at closest data point (x_p, y_p) onto the plane $x = 1/2$.

of errors between two smoothing lengths h_1 and h_2 may be made so that the order of accuracy of the method is given by

$$p \simeq \frac{\log(E(h_1)/E(h_2))}{\log(h_1/h_2)}. \tag{22}$$

This calculation remains valid provided the particles lie approximately on a regular lattice, otherwise the error may no longer be proportional to h. Calculations have shown that the development of the flow up to an approximate steady state at $T = 0.0125$ maintains this approximate regular lattice configuration.

4.2. Poiseuille flow

The use of the current method for the numerical solution of the Poiseuille flow problem can be observed in Fig. 7a which shows both the numerical and analytical solution at $x = 1/2$, i.e. $u(1/2, y, t)$ for a 64^2 grid with $h = 2.2\Delta x$. A quantitative comparison of the convergence rate can be made from Figs. 7b and 8 firstly showing log–log graphs of the L_2 error as a function of the number of particles $1/\Delta x$ and secondly as a function of smoothing length h (Fig. 8a) and the ratio of inter-particle spacing to smoothing length $\Delta x/h$ for various grid sizes (Fig. 8b).

Compare the graphs in Fig. 7b, which show the error behaviour as a function of the number of particles. Convergence is only guaranteed provided both the number of neighbours and the number of particles increase, with n always increasing faster than n_n. This

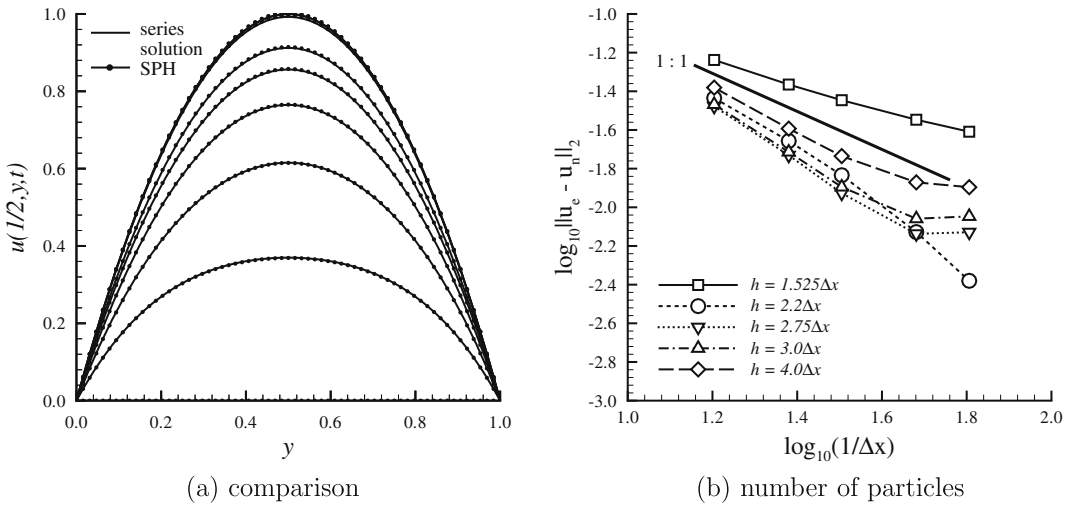

(a) comparison (b) number of particles

Fig. 7. (a) Comparison of SPH and series solutions of Poiseuille flow at $x = 1/2$ for a 64^2 grid with a smoothing length of $h = 2.2\Delta x$, (b) log–log graphs of the L_2 error for Poiseuille flow as a function of the number of particles.

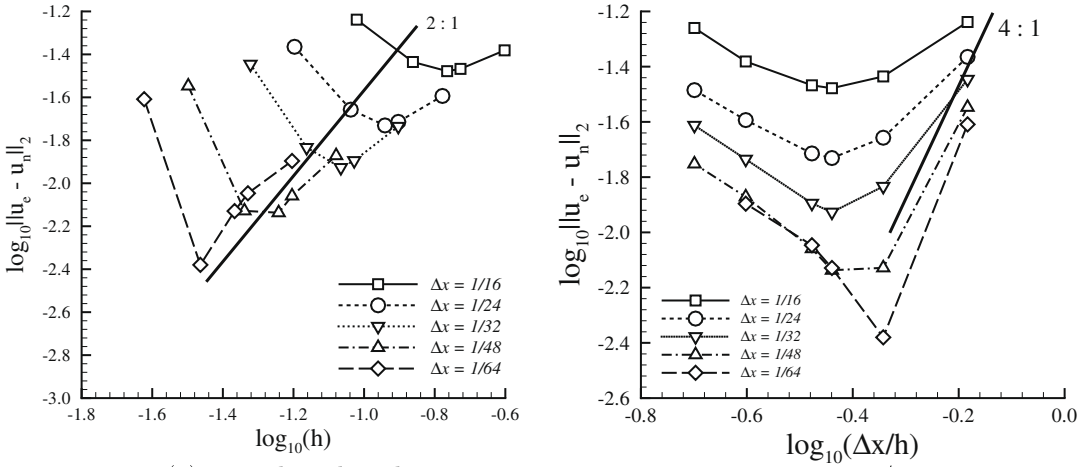

(a) smoothing length (b) $\Delta x/h$

Fig. 8. Log–log graphs of the L_2 error for Poiseuille flow as a function of (a) smoothing length and (b) $\Delta x/h$.

time, as has been shown in [5], we expect the error to converge when $E \propto O(1/\Delta x)$ resulting in slopes of order 1. Clearly, as the number of particles and neighbours increase (while still maintaining $n > n_n$), as measured by the ratio $h/\Delta x$, from $h/\Delta x = 1.525$ to $h/\Delta x = 4.0$, the slope approaches 1. This behaviour has also been observed by Graham and Hughes [5]. The graphs also demonstrate the behaviour noticed in Graham and Hughes [5] whereby second derivative errors in the viscous term are overpredicted, which effectively increases viscosity and gives rise to slopes smaller than 1 for larger numbers of particles. This behaviour is observed on the right-hand sides of the graphs. This also explains why the errors are larger for values of $h/\Delta x$ beyond 2.2.

Fig. 8a shows that second order convergence (as shown by the line marked 2:1) is approached for the finer grids $\Delta x = 1/48, 1/64$, or equivalently for larger numbers of particles as h decreases. The graphs also display the typical behaviour pointed out by [14] when discretisation error dominates the smoothing error giving rise to negative slopes on the left hand side of the graphs, i.e. for $h/\Delta x = 1.525, 2.2$. The graphs show that a minimum in the error is reached, at about $h/\Delta x \simeq 2.7$, after which the error becomes progressively dominated by the smoothing error and the slopes become positive. As both Δx and h are decreased, so that $h/\Delta x$ gets larger, increasingly improved convergence rates are obtained which approach second order. From Fig. 8a we see that even though the error progressively decreases as the initial inter-particle spacing Δx is reduced from $\Delta x = 1/16$ to $\Delta x = 1/32$, the further reduction from $\Delta x = 1/48$ to $\Delta x = 1/64$, actually increases the error demonstrating the interaction between the smoothing error $O(h^2)$ and discretisation error $O[(\Delta x/h)^{\beta+2}]$ terms as shown in Quinlan et al. [14].

Fig. 8b shows how the L_2 error varies with the ratio $\Delta x/h$. Given that $\beta = 2$ for the kernel used in this paper we expect to see error behaviour of the form $(\Delta x/h)^4$ which can be observed on the right-hand side of Fig. 8b when the ratio $\Delta x/h$ is large and h small.

Fig. 9 shows how the error grows with time to its final value at $T = 0.0125$. The figure shows both the $h = 1.525\Delta x$ and the $h = 3\Delta x$ results to judge how the smoothing length/grid size ratio affects error growth. Clearly, as the ratio $h/\Delta x$ increases with finer grid resolution Δx, the final steady state error obtained at $t = T$ is both smaller and is reached more quickly than for the larger ratios. The $h = 1.525\Delta x$ case involves an initial drop and then a growth in error for almost half the time until the steady state is reached

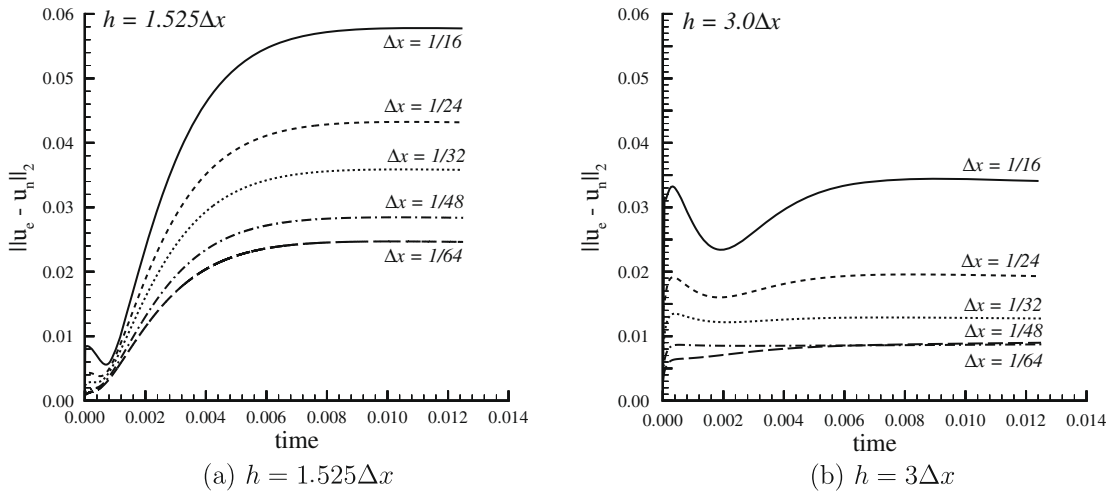

Fig. 9. Time variation of the L_2 error for Poiseuille flow for various grids.

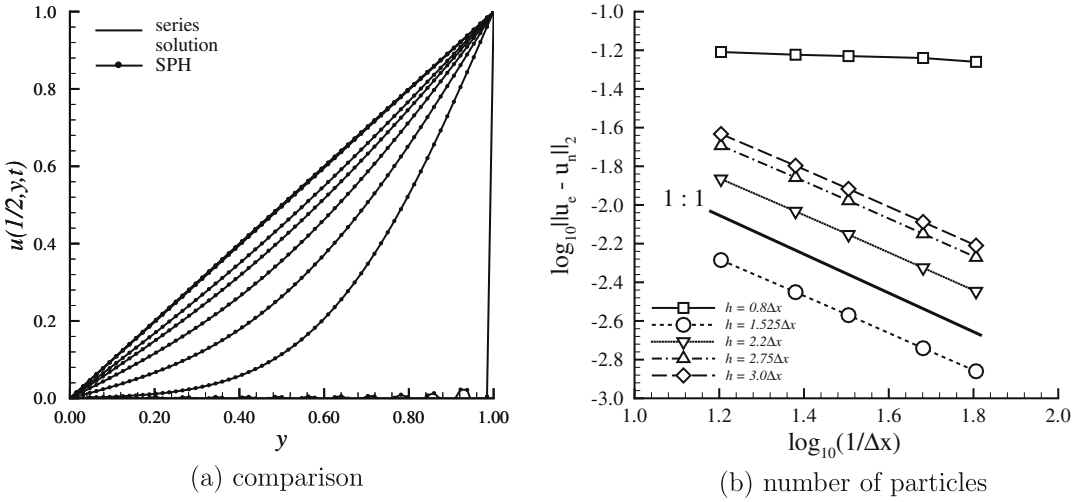

Fig. 10. (a) Comparison of SPH and series solutions of Couette flow at $x = 1/2$ for a 64^2 grid with a smoothing length of $h = 3\Delta x$, (b) log–log graphs of the L_2 error for Couette flow as a function of the number of particles.

whereas the $h = 3\Delta x$ case has a prolonged error drop followed by error growth although still reaching the final steady state at about the same time.

The limiting behaviour of Fig. 9 suggests that the expression of Shao and Lo [17] is subject to errors of order one and so there is no real advantage in using it instead of the expression in [11] for the problems considered here.

4.3. Couette flow

From Fig. 10a, using a 64^2 grid and $h = 3\Delta x$, it is clear that, like the Poiseuille case, the SPH solution closely approximates the analytical solution. Fig. 10b demonstrates slopes of order 1 for the error as a function of the number of particles for the entire range of $h/\Delta x$ ratios and number of particles. Note, however, that for a given number of particles, as the ratio of the number of neighbours to the number of particles $n_n/n \simeq 4h$ increases, the error also increases. This characteristic was true for the Poiseuille case only for ratios $h/\Delta x > 2.2$. Note also that the graph for $h = 0.8\Delta x$ does not show a slope of order one, rather, a much smaller slope so that the error appears to be almost independent of the number of particles for this ratio of smoothing length to inter-particle spacing. This decrease in slope was also true to a lesser degree in the Poiseuille flow case, cf the $h = 1.525\Delta x$ graph in Fig. 7b with the other cases.

Fig. 11a shows the convergence behaviour as a function of smoothing length. Almost second order convergence is observed for all grid spacings and larger smoothing lengths. The case when $h = 0.8\Delta x$, corresponding to the most negative value of $\log_{10}(h)$ for each graph, shows how the ratio of inter-particle spacing to smoothing length dominates the smoothing length in this region (cf h and $\Delta x/h$ in each case).

Fig. 11b demonstrates the influence of discretisation error for larger values of $\Delta x/h$ on the right-hand side of each graph. Here, the slopes approach order 4 as expected from the analysis of Quinlan et al. [14]. It should be pointed out that the $O(h^2)$ and $O[(\Delta x/h)^4]$ error behaviour for both the Poiseuille and Couette flow problems follows similar trends with a characteristic V shape to the graphs of E versus h and $\Delta x/h$. However, the minimum in the V shaped graph is reached at different values of $h/\Delta x$ for the two flow problems with $h/\Delta x \simeq 2.7$ for the Poiseuille case and $h/\Delta x \simeq 1.5$ for the Couette case. Similarly, the $O[(\Delta x/h)^4]$ behaviour of the discretisation error is demonstrated for the finer grids in the Poiseuille flow case but shows up better for the coarser grids for the Couette flow case. Fig. 12 shows the time variation of the error for the $h/\Delta x = 1.525, 3.0$ ratios. It again shows how a larger ratio of n_n/n

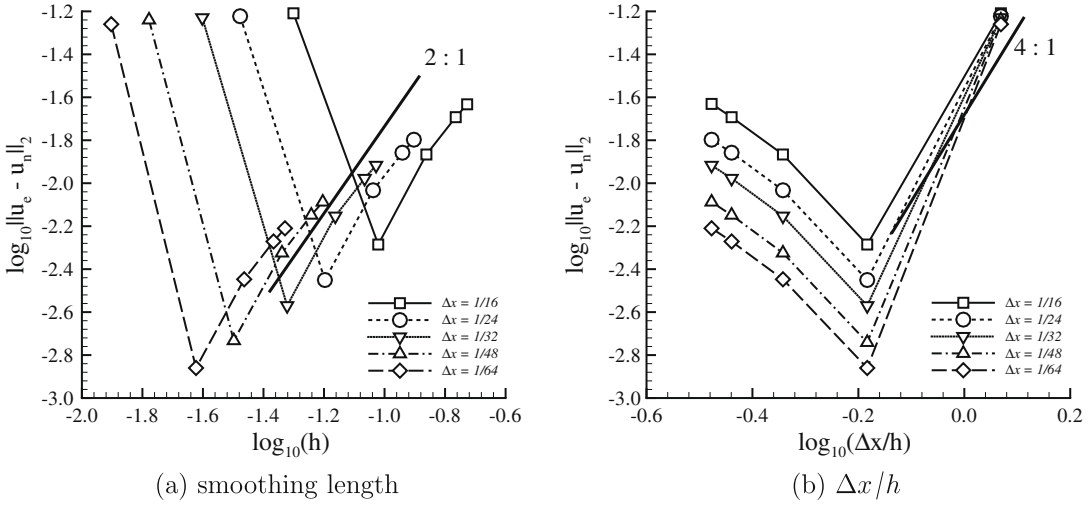

Fig. 11. Log–log graphs of the L_2 error for Couette flow as a function of (a) smoothing length and (b) $\Delta x/h$.

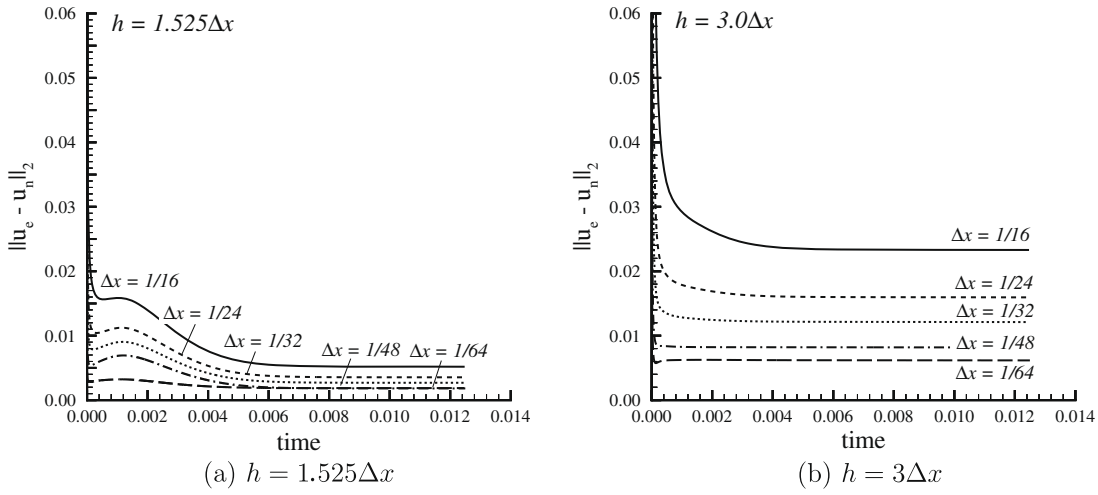

Fig. 12. Time variation of the L_2 error for Couette flow for various grids.

increases the error. It also shows that larger ratios of $h/\Delta x$ reach the asymptotic solution faster than smaller ones.

5. Conclusion

A new approach to the implementation of boundary conditions in the method of smoothed particle hydrodynamics has been presented. This approach has allowed the accurate simulation of incompressible flows for low Reynolds numbers.

The proposed method provides a solution to the so-called particle deficiency problem. This problem arises in the vicinity of rigid walls and is due to insufficient information being available to perform accurate interpolation of data at particles located nearer to the boundary than the support of the interpolation kernel. The proposed method differs from other approaches that have used image particles to overcome the particle deficiency problem. Many of these alternative techniques require a large number of image particles to obtain accurate approximations. The velocity of image particles is obtained using linear extrapolation. The consistent reflected image particle method possesses two main advantages

- no extra image particles must be stored as part of the code. All image particles are constructed from and are co-moving with matching domain particles about a no-slip boundary so that image particle velocities are integral and not offset.
- image particle velocities are consistent with both the no-slip boundary conditions and the momentum equations improving the order of accuracy compared to previous interpolation approaches.

The consistent reflected image particle approach is validated on two benchmark problems, viz. Poiseuille flow and Couette flow. The number of particles and the smoothing length are varied and the accuracy of the approximation as a function of these parameters is investigated.

This paper represents a first stage in the application of the consistent reflected image particle approach used here to solve problems with SPH which include no-slip boundaries. Future work will apply the method to more general problems such as flow around immersed bodies. Note that the use of the method to model no-slip boundaries immersed within the flow having irregular geometries remains valid for particles located within the immersed body. The same reflected image approach may be used to evaluate image particle velocities and the momentum equation may be implemented using a localised $x - y$ coordinate frame with tangential and normal directions at each boundary point.

Acknowledgements

The authors would like to acknowledge the financial support of the EPSRC (Engineering and Physical Sciences Research Council) of the United Kingdom through Grant EP/C513037.

The authors are indebted to one of the referees for their constructive comments which have improved the quality of the paper.

References

[1] P. Artymowicz, S.H. Lubow, Dynamics of binary-disk interaction. 1. Resonances disk gap sizes, Astrophys. J. 421 (1994) 651–667.
[2] J. Campbell, R. Vignjevic, L. Libersky, A contact algorithm for smoothed particle hydrodynamics, Comput. Methods Appl. Mech. Engrg. 184 (2000) 49–65.
[3] J. Fang, R.G. Owens, L. Tacher, A. Parriaux, A numerical study of the SPH method for simulating transient viscoelastic free surface flows, J. Non-Newtonian Fluid Mech. 139 (2006) 68–84.
[4] R.A. Gingold, J.J. Monaghan, Smoothed particle hydrodynamics: theory and application to non-spherical stars, Mon. Not. R. Astron. Soc. 181 (1977) 375–389.
[5] D.I. Graham, J.P. Hughes, Accuracy of SPH viscous flow models, Int. J. Numer. Math. Fluids 56 (2008) 1261–1269.
[6] S. Li, W.-K. Liu, Meshfree and particle methods and their applications, Appl. Mech. Rev. 55 (2002) 1–34.
[7] J.J. Monaghan, Smoothed particle hydrodynamics, Ann. Rev. Astron. Astrophys. 30 (1992) 543–674.
[8] J.J. Monaghan, Simulating free surface flows using SPH, J. Comput. Phys. 110 (1994) 399–406.
[9] J.J. Monaghan, Smoothed particle hydrodynamics, Rep. Prog. Phys. 68 (2005) 1703–1759.
[10] J.J. Monaghan, A. Kocharyan, SPH simulation of multi phase flow, Comput. Phys. Commun. 87 (1995) 225–235.
[11] J.P. Morris, P.J. Fox, Y. Zhu, Modeling low Reynolds number incompressible flows using SPH, J. Comput. Phys. 136 (1997) 214–226.
[12] L. Oger, S.B. Savage, Smoothed particle hydrodynamics for cohesive grains, Comput. Methods Appl. Mech. Engrg. 180 (1999) 169–183.
[13] D.J. Price, Magnetic Fields in Astrophysics, PhD Thesis, University of Cambridge, Cambridge, 2004.
[14] N.J. Quinlan, M. Basa, M. Lastiwka, Truncation error in mesh-free particle methods, Int. J. Numer. Methods Engrg. 66 (2006) 2064–2085.
[15] P.W. Randles, L.D. Libersky, Smoothed particle hydrodynamics: some recent improvements and applications, Comput. Methods Appl. Mech. Engrg. 139 (1996) 375–408.
[16] F.A. Rasio, Particle methods in astrophysical fluid dynamics, Prog. Theor. Phys. Supp. 138 (2000).
[17] S. Shao, E.Y.-M. Lo, Incompressible SPH method for simulating Newtonian and non-Newtonian flows with a free surface, Adv. Water Resour. 26 (2003) 787–800.
[18] L.D. Sigalotti, J. Klapp, E. Sira, Y. Melean, A. Hasmy, SPH simulations of time-dependent Poiseuille flow at low Reynolds numbers, J. Comput. Phys. 191 (2003) 622–638.
[19] H. Takeda, S.M. Miyama, M. Sekiya, Numerical simulation of viscous flow by smoothed particle hydrodynamics, Prog. Theor. Phys. 92 (1994) 939–959.